Monte Carlo Simulation of the Effect of Entanglements on the Swelling and Deformation Behavior of End-Linked Polymeric Networks

Zhong Chen, Claude Cohen, and Fernando A. Escobedo*

School of Chemical Engineering, Cornell University, Ithaca, New York 14850-5201

Received November 26, 2001; Revised Manuscript Received February 6, 2002

ABSTRACT: The effect of entanglements on deformation properties of end-linked networks was investigated using Monte Carlo simulations. Model tetrafunctional networks were prepared by cross-linking precursor monodisperse chains in the framework of the bond fluctuation model (BFM). The degree of entanglement in these networks was tuned by changing the precursor chain lengths ($N = 20$ and 50-mers) and the initial polymer concentration (Φ_0). Continuum-space simulations of isotropic swelling and uniaxial deformation were carried out in isobaric and isostress ensembles, respectively. Both equilibrium swelling and force-strain data indicated that elastic forces are enhanced in more entangled networks. The effect of Φ_0 on the equilibrium swelling and on the elastic modulus was analyzed with the help of scaling theory and the Rubinstein and Panyukov model, respectively; our results are shown to be consistent with reported experimental data. Our results indicate that the effect of entanglements on the network elastic response is the largest at small extension and decreases with strain at higher extensions (supporting an entanglement-slippage scenario).

1. Introduction

The unusual elasticity of rubberlike materials originates in their cross-linked polymeric structure. The stress in a deformed elastomer is essentially due to entropy changes of the network chains whose conformations are constrained and cannot fully relax upon a macroscopic deformation. By treating a piece of elastomer as a collection of entropic springs that deform proportionally with macroscopic deformation, the earliest molecularly based theories, including the affine[1,2] and phantom models,[3,4] are relatively successful in describing the behavior of real networks at small strains. Because these models neglect excluded-volume interactions, they can only qualitatively predict the shape of the stress−strain curve. The impenetrability of network chains also gives rise to trapped entanglements which act as topological constraints that also affect elastic behavior. The precise role of entanglements in network elasticity has long been controversial, and many theories have been proposed to account for it. Classical theories of rubber elasticity assume that entanglements simply restrict the fluctuations of cross-links,[5−9] while tube models emphasize the importance of the topological constraints acting along the contour of strands exceeding a minimum "entanglement length", N_e.[10−14]

Despite numerous efforts, a rigorous statistical mechanical treatment of network entanglements remains elusive. Computer simulation, on the other hand, has proven to be a very useful tool to study this problem not only by providing data to test theories but also by readily bridging macroscopic deformation behavior to conformational properties of the chains. In some coarse-grained models, the network chains are treated as random walks connecting several (entanglements) nodes; although such models do not include details of chain configuration between nodes, they can be designed to capture the effect of entanglements on deformation behavior.[15] More detailed network models have been adopted to rigorously account for the excluded volume of effective monomers, the conservation of topology, and the noncrossability of network strands. The effect of entanglements in network properties was investigated in a series of molecular dynamic (MD) simulations of end-linked polymer networks by Kremer et al. These authors calculated the elastic modulus employing two alternative routes: by a Rouse mode analysis in the unstrained state[16,17] and by monitoring the network relaxation upon a small deformation (initiated by an affine change of coordinates).[18,19] Holtz et al. adopted an on-lattice model[20] wherein the stress−strain curve was simulated by resorting to simple extensional experiments; analysis of the chain structures revealed pronounced nonaffine deformation behavior. Everaers[21] carried out MD simulations on networks with diamond lattice connectivity, where the effect of entanglements was separated from other sources of trapped disorder. In this way, this author was able to investigate the influence of topological constraints on the local dynamics in cross-linked polymer melts and on the elastic properties.

Early simulation works of network swelling[22,23] were performed using the canonical (constant NVT) ensemble where a "chunk" of network is swollen by placing it in larger and larger lattices wherein empty sites play the role of solvent molecules. More realistic simulations on the swelling of athermal gels have been carried out by employing an osmotic ensemble in a continuum space and with solvent molecules explicitly modeled.[24−26] An on-lattice isobaric−isothermal (NPT) ensemble has been used to investigate the uniaxial swelling and deswelling of end-linked networks[27] by employing the bond fluctuation model (BFM).[28,29] To the best of our knowledge, the correlation between the degree of network entanglements and swelling equilibria has not been investigated via molecular simulation.

The goal of this work is to investigate the effect of the degree of entanglement on the elastic properties of end-linked networks, in particular, the effect of initial concentration of precursor chains during the curing process. The effect of precursor concentration and precursor molecular weight on the modulus and swelling of poly(dimethylsiloxane) (PDMS) networks have been studied experimentally and analyzed in the context of scaling theories.[30] This work is complementary to such

10.1021/ma012048i CCC: $22.00
Published on Web 03/09/2002

an experimental−theoretical study in that it provides further evidence of the dependence of elastic properties on the degree of entanglement and gives a detailed account of the relation between micro- and macroscopic behavior. It also complements a previous simulation study where the effect of precursor concentration on cross-link mobility was observed.[31] The model networks employed in this work were prepared at different precursor concentrations while tuning reaction conditions to minimize structural differences. In this way, the degree of entanglement can be varied and its effect on elasticity be isolated from that of chemical cross-linking. Simulations of network swelling and uniaxial extension were carried out using the NPT and isostress ($NP_zP_{xy}T$) ensembles, respectively; these simulations allowed the direct determination of swelling equilibrium, stress−strain curves, and conformational properties of network chains. Two key aspects distinguish our work from others: (1) the effect of entanglements is investigated in networks of realistic architecture (i.e., end-linked networks formed by cross-linking reactions) wherein the degree of entanglement is purposely varied, and (2) the uniaxial extension and compression are simulated in a continuum space model and an isostress ensemble which closely mimics actual deformation experiments. By allowing a direct quantification of entanglement effects on elastic behavior, our results support the idea that entanglements act like chemical cross-links at small deformations but then appear to "soften" at higher strains, arguably, because of the mobility (slippage) of chains around entanglement points.

2. Simulation Methodology

2.1. Preparation of Sample Networks. The sample networks of athermal 20-mers and 50-mers were prepared in the framework of the three-dimensional BFM in a lattice system with periodic boundaries in all three directions. The details of the formation of end-linked networks can be found elsewhere.[32] All systems have 612 chains and 337 tetrafunctional cross-links; the ratio of cross-link sites to precursor polymer chain ends is chosen to be $r = 1.1$, which is close to the optimal ratio (one that minimizes topological defects) found in a previous simulation study.[32] The networks are formed at three different concentrations $\Phi_0 = 1.0$, 0.70, and 0.51, where Φ_0 is defined as a volume fraction:

$$\Phi_0 = \frac{\phi_0}{\phi_{\mathrm{melt}}} \tag{1}$$

where $\phi = 8vN_t/V$ is the fraction of occupied volume in the lattice, $N_t = nN + C$ is the total number of monomers in the system, N is the number of monomers per precursor chain, n is the number of precursor chains, C is the number of cross-links, v is the volume of a lattice site, V is the lattice volume, and 8 is the number of lattice sites that each repeat unit occupies. ϕ_0 is the value of ϕ at the actual conditions of network formation, and ϕ_{melt} is the value of ϕ corresponding to a meltlike density in the BFM;[28] in this work we adopted $\phi_{\mathrm{melt}} = 0.47$. Systems with $\Phi_0 < 1$ then correspond to solution conditions wherein $(1 - \Phi_0)$ is the volume fraction of solvent.

After the multichain system is well equilibrated at the desired volume fraction, curing is allowed by forming bonds when an unsaturated chain end and a cross-link move into neighboring positions. The cure process is stopped when a negligible soluble fraction (<0.5%) and a large percentage of elastic material (>90%) are reached. The curing times (total number of MC steps) for networks formed at different Φ_0 were varied in order to obtain systems with similar structural characteristics, in particular, to get nearly equal number of elastic chains. Key structural features of the samples studied are listed in Table 1.

Table 1. Network Structural Properties of the Systems Used in the Deformation Studies[a]

	N_d	N_{loop}	w_{sol}	w_{loops}	w_{pend}	w_{elast}
20-mer						
$\Phi_0 = 0.51$	7	29	0.0033	0.047	0.040	0.910
$\Phi_0 = 0.70$	5	34	0.0017	0.054	0.042	0.903
$\Phi_0 = 1.00$	9	35	0.0033	0.056	0.038	0.903
50-mer						
$\Phi_0 = 0.51$	6	24	0.0016	0.039	0.035	0.924
$\Phi_0 = 0.70$	23	13	0.0033	0.021	0.052	0.924
$\Phi_0 = 1.00$	12	22	0.0032	0.036	0.035	0.925

[a] N_d is the number of dangling chains, N_{loops} is the number of loops, w_{sol} is the soluble fraction, w_{elast} is the fraction of the elastically effective material, w_{pend} is the fraction of pendent material, and w_{loops} is the fraction of single-chain loops attached to the elastic network. Detailed definitions of these structures can be found in ref 32.

While almost all simulations reported in this work refer to networks formed by the reactive scheme described above, a few simulations were performed with "diamond" networks for comparison purposes. Diamond networks represent a limiting entanglement-free idealization of a tetrafunctional network wherein all cross-links are saturated, and if all chains were fully stretched, the cross-links would lie at the nodes of a diamond lattice.

2.2. Network Deformation. In contrast to network formation, we utilize a continuum-space network model for deformation simulations. This choice is mainly motivated by the ease with which volume moves can be implemented in an off-lattice system; furthermore, packing and short-range structural properties tend to be more realistic in continuum-space chains. The coarse-grained chain monomers and the cross-links are modeled as beads of uniform diameter σ. The bond length bl is allowed to fluctuate within a range: $\sigma - \Delta bl \le bl \le \sigma + \Delta bl$ where $\Delta bl = 0.2\sigma$; this model can be seen as a continuum-space counterpart of the on-lattice BFM. Nonbonded beads interact via a purely repulsive Lennard-Jones (LJ) potential:

$$U_{\mathrm{LJ}}(r) = \begin{cases} 4\epsilon\left\{\left(\frac{\sigma}{r}\right)^{12} - \left(\frac{\sigma}{r}\right)^{6} - \left(\frac{\sigma}{r_c}\right)^{12} + \left(\frac{\sigma}{r_c}\right)^{6}\right\}, & r \le r_c \\ 0, & r > r_c \end{cases} \tag{2}$$

where r is the distance between two beads, $r_c = 2^{1/6}\sigma$, and ϵ is the LJ energy parameter which was set such that the reduced temperature, k_BT/ϵ, is unity (k_B is Boltzmann's constant). This "repulsive" molecular model is intended to describe a polymer network in a good "implicit" solvent; i.e., the preference of polymer beads to be surrounded by solvent gives rise to an effective repulsive interaction among polymer beads. Note also that each bead represents several actual repeat units in a real polymer.

The lattice coordinates of each BFM network (obtained by the cure process described earlier) were transformed into the coordinates of the off-lattice system by first rescaling the simulation box lengths to attain uniformity in bead size and then relaxing the system to bring all bond lengths within specification (i.e., into

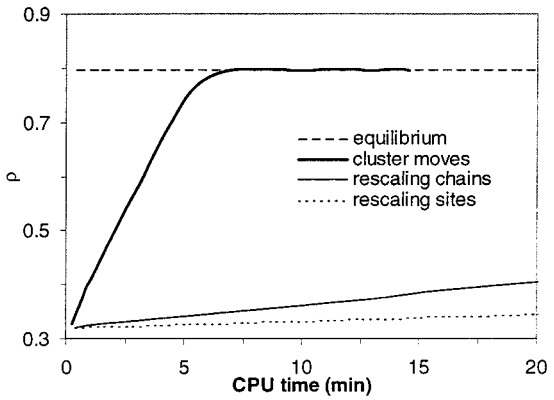

Figure 1. Evolution of the bead-number density of a network (made up of 612 20-mer chains) as a function of CPU time (in a 633 MHz 164-alpha processor) upon the application of a step increase in pressure. The performance of three volume-move algorithms for (isotropic) NPT ensemble simulations are tested: cluster moves, site-rescaling, and chain-rescaling moves.

the range $\sigma - \Delta bl \leq bl \leq \sigma + \Delta bl$). Note that network topology and chain structure are preserved upon this transformation.

Molecular rearrangements (for thermal equilibration) in the off-lattice system were achieved via hopping moves (similar to those employed in BFM simulations). In a hopping move, a randomly selected bead is displaced in a random direction and by a random distance; the new position is accepted or rejected depending on the energy change according to the conventional Metropolis criterion (a move is rejected if a bond length falls out of the allowed range). Note that these moves are effective even for tri- and tetrafunctional sites. Besides single-bead hopping moves, flipping moves (random rotation of one bead along the line connecting the centers of mass of its two neighbors) were employed to rearrange bifunctional sites.

Network deformation requires the use of "volume" moves that change the dimensions of the box (to attain mechanical equilibration). Conventional volume moves,[33] however, are not directly applicable to networks because such moves require the presence of decoupled molecules whose center-of-mass positions can be rescaled with the box size. (Networks are coupled not only by cross-links but also by the periodic boundary conditions.) Cluster volume moves[25] were used here for their proven efficiency to deform networks. In a cluster volume move, sites in network strands are temporarily deleted (i.e., left dangling) so that the network becomes a set of uncoupled star-shaped clusters that can be repositioned as in a conventional volume move. Afterward, the dangling sites are reattached to the corresponding strands to preserve the network topology (and trapped entanglements). At least two other types of volume moves can be implemented for our networks that take advantage of the fluctuating nature of the bond length. One of them is the simple site-rescaling approach, where the coordinates of all sites are rescaled according to the volume change. The other is a chain-rescaling approach, where the cross-links are chosen as dangling sites so that the centers of mass of network chains can be rescaled. The relative efficiency of all these methods was tested via NPT simulations for a 20-mer network (612 chains) formed at $\Phi_0 = 0.51$, where the change in bead number density ρ [$= N_t/V$] was monitored after a step-function change in pressure. Figure 1 shows that cluster volume moves provide about 2 orders of magnitude faster mechanical equilibration than either site-rescaling moves or chain-rescaling moves.

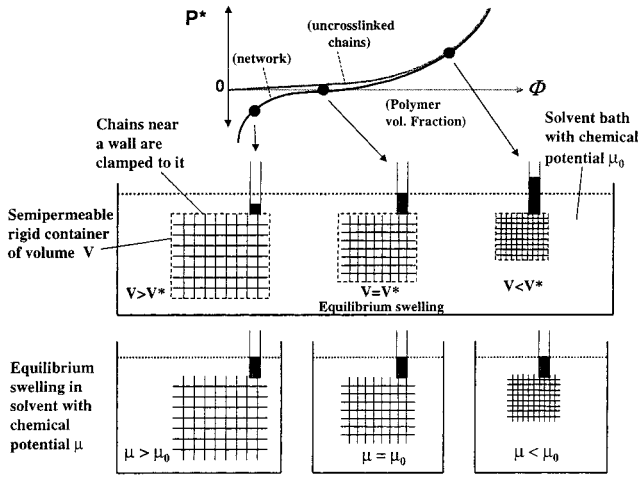

Figure 2. Schematic picture illustrating the qualitative relation between osmotic pressure (P^*) and polymer volume fraction for a polymer solution (un-cross-linked chains) and for a polymer network. The osmotic pressure becomes the total pressure in a model system where the solvent is not explicitly simulated (i.e., with an *implicit* solvent). Different degrees of swelling can be seen as resulting from (i) constrained swelling (controlled by the volume of a suitable container) which gives rise to different osmotic pressures or, equivalently, (ii) the equilibrium swelling ($P^* = 0$) of the network in solvents of different chemical potential.

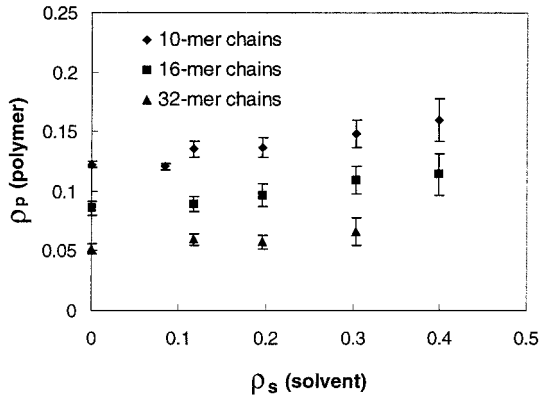

Figure 3. Equilibrium swelling of off-lattice athermal model networks (with different precursor chain lengths) as a function of the density of solvent phase. Data presented here are derived from simulation data presented in ref 25 where an osmotic ensemble and an explicit monomeric solvent were employed.

For swelling simulations, a uniform osmotic pressure $P^* = P\sigma^3/\epsilon$ is applied in all three directions. The idea that the swelling of a network in the presence of an *implicit* solvent can be controlled via P^* is illustrated in Figure 2. The conditions of equilibrium swelling are seen to correspond to $P^* = 0$. The validity of such an approximation can be tested by reexamining the reported equilibrium swelling data of athermal diamond networks with an explicit monomeric solvent.[25] If the monomer fluid is a good solvent regardless of its density, then the polymer number density in the swollen network [ρ_p] should be approximately the same as that of a pure network (with implicit solvent) at $P^* = 0$. Figure 3 shows such a comparison; clearly, ρ_p is not very sensitive to explicit solvent number density [ρ_s], and the values for $\rho_s = 0$ provide a slightly larger swelling (i.e., an implicit solvent behaves as a mildly better solvent than the monomeric fluid at finite densities).

For the uniaxial deformation runs, the off-lattice samples (with adjusted bond lengths) were equilibrated at a melt density (bead number density of $\rho \approx 0.8$) by performing an isotropic NPT simulation at a high pressure $P^* = 3.0$. During the uniaxial stretching simulations, the pressures along x and y directions, P_x and P_y, are kept constant at 3.0, while a smaller pressure is applied in the z direction (P_z). The reduced value of P_z will force the sample to stretch along the z direction in a manner that is analogous to a real simple extension experiment. If P_z is larger than P_x and P_y, then a uniaxial compression is achieved. Since the net stress σ_T along the z direction is $(P_x + P_y)/2 - P_z$, the force applied on the sample is

$$f = \sigma_T L_x L_y \tag{3}$$

where L_x and L_y ($= L_x$) are the dimensions of the network sample in x and y direction, respectively. While L_x, L_y, and L_z change significantly during a deformation simulation, the network volume ($V = L_x L_y L_z$) was observed to vary almost negligibly (<0.6%) for all strain ratios probed by our simulations; this indicates that our model system behaves properly as a nearly incompressible material.

Under deformation, the components of the end-to-end distance of the elastic chains can be expressed as

$$\langle R_{e,xy}{}^2 \rangle = \lambda_{xy,m}{}^2 \langle R_{e,xy}{}^2 \rangle_0, \quad \langle R_{e,z}{}^2 \rangle = \lambda_{z,m}{}^2 \langle R_{e,z}{}^2 \rangle_0 \tag{4}$$

where $\langle R_{e,xy}{}^2 \rangle$ is the mean-square end-to-end distance, $\lambda_{xy,m}$ and $\lambda_{z,m}$ are the microscopic deformation ratios in the x, y directions and z direction, respectively, and subscript zero denotes the undeformed state. The macroscopic deformation ratio can be determined from the dimensions of the network before ($L_{z,0}$) and after (L_z) deformation using

$$\lambda = \frac{L_z}{L_{z,0}} \tag{5}$$

The components of mean-square radius of gyration in the strain direction $\langle R_{g,z}{}^2 \rangle$ and in the transversal direction $\langle R_{g,xy}{}^2 \rangle$ at different deformation ratios were also collected during the simulation.

A net orientation of chain segments along the strain axis can occur when a network is uniaxially stretched; this net alignment can be detected by the segmental order parameter S, which can be calculated as

$$S = \langle P_2(\cos \theta) \rangle \tag{6}$$

where θ is the angle between the orientation of chain segments and the strain axis, P_2 is the second Legendre polynomial, and the average is over all the segments and over the whole simulation time. By assuming affine deformation and Gaussian chain statistics, Kuhn and Grun[34] found that

$$S \propto (\lambda^2 - \lambda^{-1}) \tag{7}$$

3. Results and Discussion

3.1. Undeformed Networks. We examine here the effect of entanglements on the mobility of cross-links and inner chain sites in a network. Since entanglements tend to constrain the fluctuations of all beads in the system, networks cured at different Φ_0 (i.e., having dissimilar degree of entanglements) should exhibit different relaxation dynamics. Although such a difference was observed in an earlier MD simulation study,[31] that study was not conclusive because the two networks employed were quite small in size and lacked uniformity in fraction of elastic material. Here, our 612-chain 50-mer networks prepared at three different values of Φ_0 (but having the same fraction of elastic chains) were first brought to the same meltlike density ($\rho \approx 0.8$). The networks were then relaxed using off-lattice canonical ensemble MC simulations to monitor the motion of the cross-links via the time-dependent mean-squared displacement (MSD), $g_x(t)$:

$$g_x(t) = \langle [r_i(t + t_0) - r_i(t_0)]^2 \rangle \tag{8}$$

where the brackets denote average over all saturated cross-links and over "time" origins. The "time" t is taken here to correspond to simulation duration in units of MC cycles; because only one-bead moves were used to relax the system, the number of MC cycles is approximately proportional to the "real time". A measure of the mobility of elastic chains is given by $g(t)$, the MSD of the monomer located at the middle of the chain. It is seen in Figure 4a that at short times $g_x(t)$ and $g(t)$ increase with time following Rouse dynamics, i.e., $g_x(t)$, $g(t) \sim t^{1/2}$ (as could be readily seen in a log−log plot), while at longer times the curves begin to level off.[17] Even though our simulations were not long enough to reach

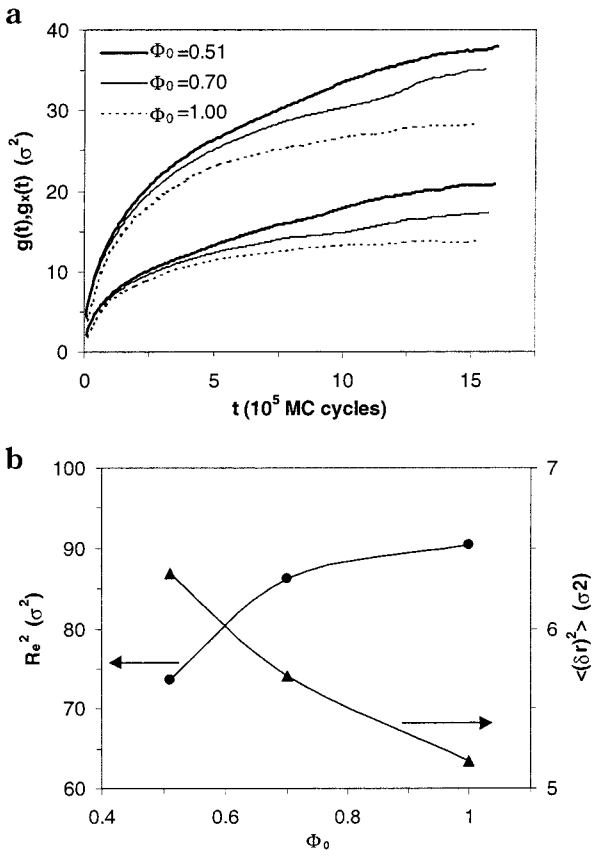

Figure 4. (a) Mean-squared displacement of the chain middle sites $g(t)$ (upper curves) and of the cross-links $g_x(t)$ (lower curves) as a function of MC cycles for 50-mer networks in the undeformed state (in a MC cycle, all sites are moved in average once). (b) Mean-squared end-to-end distance $R_e{}^2$ and average displacement of cross-links from their mean positions $\langle(\delta r)^2\rangle$ as a function of precursor concentration (Φ_0) for the 50-mer networks from frame (a).

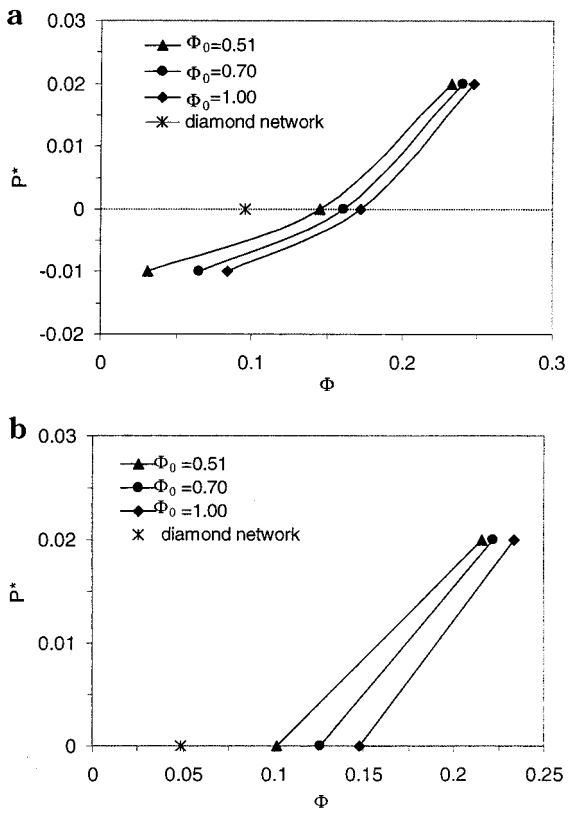

Figure 5. Simulated osmotic pressure P^* vs network volume fraction Φ for the isotropic swelling of networks formed at different initial conditions: (a) 20-mer networks and (b) 50-mer networks. The error bars of the volume fraction (not shown) are smaller than the data symbols. The solid lines are drawn as guides for the eye.

the plateau values of $g_x(t\rightarrow\infty)$ and $g(t\rightarrow\infty)$,[17,31] it is clear that the MSDs of cross-links and elastic chains are smaller for larger Φ_0. Figure 4b shows that the MSD of a cross-link with respect to its mean position, $\langle(\delta r)^2\rangle$, also decreases as Φ_0 increases. Such a reduction in bead mobility for larger Φ_0 can be attributed to the increase of trapped entanglements with Φ_0. Figure 4b further shows that the mean-squared end-to-end distance of network chains increases with Φ_0. This is because chains cross-linked at a lower Φ_0 collapse onto themselves more when they are brought to melt density; more collapsed chains are less interpenetrated with others, which could correlate with higher bead mobilities.

3.2. Swelling. Swelling results are reported in terms of the network volume fraction Φ (with respect to the volume of network plus solvent), which for an off-lattice system with implicit solvent can be estimated in a manner similar as in eq 1, i.e.,

$$\Phi = \frac{\rho}{\rho_{\text{melt}}} \tag{9}$$

where ρ [$= N_t/V$] is the network bead-number density. In our systems, we adopted for ρ_{melt} the density for the "dry" network before deformation ($\rho_{\text{melt}} \approx 0.8$). Note that the volume of the swollen network is proportional to Φ^{-1}. Figure 5a shows our isotropic NPT results near zero pressure for 20-mer networks formed at three values of Φ_0: 1.0, 0.70, and 0.51. As expected, for all samples Φ decreases as P^* is reduced. The significance of negative pressures has been discussed elsewhere,[24] and Φ values for $P^* < 0$ may be interpreted as

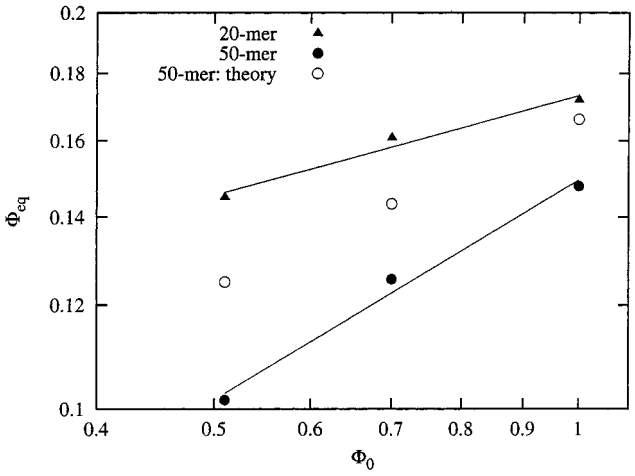

Figure 6. A log−log plot of the equilibrium swelling volume fraction (Φ_{eq}) as a function of precursor chain concentration at curing (Φ_0). The slope of the best-fit straight line increases from 0.25 for 20-mer networks to 0.55 for 50-mer networks. Predictions from a modified Flory−Rehner equation for 50-mer networks are also shown (○).

equilibrium swelling values of the network in a solvent of higher chemical potential.[35] It is clearly observed that, at the same P^*, the network prepared at higher Φ_0 swells less. Considering the similarity of chemical structure among samples, the difference in swelling behavior can only be explained by the difference in the extent of entanglements trapped during curing. A network cured at a higher Φ_0 more readily traps entanglements than one cured at a lower Φ_0; more entanglements entail less swelling. For the BFM (with which the network samples are first generated), the melt entanglement length is $N_e \approx 38$.[23,29] Even though the chain length of the 20-mer is only about half of N_e, the effect of entanglements on network swelling is significant already. This can be explained by the fact that the concentrations of the initial polymer solutions are beyond the critical overlap concentration c^*, and chains begin to intersperse with each other. In fact, the number of chains in a volume $^4/_3\pi(R_g)^3$ is found to be 1.3 for the most dilute 20-mer solution ($\Phi_0 = 0.51$). Once those chains are end-linked, their interpenetration will be partially fixed in the form of entanglements that will impact the swelling behavior. Similar results were also obtained for 50-mer networks, as shown in Figure 5b.

The values of Φ at equilibrium swelling ($P^* = 0$), to be denoted as Φ_{eq}, are also plotted for entanglement-free diamond networks in Figure 5. These diamond networks, despite having no defects (i.e., all chain are elastic), swell significantly more than even the networks cross-linked at the lowest Φ_0 (=0.51); this difference is more pronounced for the 50-mer networks where the diamond network swells twice as much as the network formed at $\Phi_0 = 0.51$.

The values of Φ_{eq} for 20-mer and 50-mer networks are plotted against Φ_0 in Figure 6. At the same Φ_0, 20-mer networks swell less because of their higher cross-link density. For the same change in Φ_0, the 50-mer networks exhibit a larger change in Φ_{eq} than the 20-mer networks; this result is consistent with experimental findings[30] and is due to the greater extent of trapped entanglements in longer chains compared to shorter chains. In fact, since the overlap concentration scales as $c^* \sim N^{-0.8}$, 50-mer chains overlap more strongly (and thus entangle more) than 20-mer chains at the same

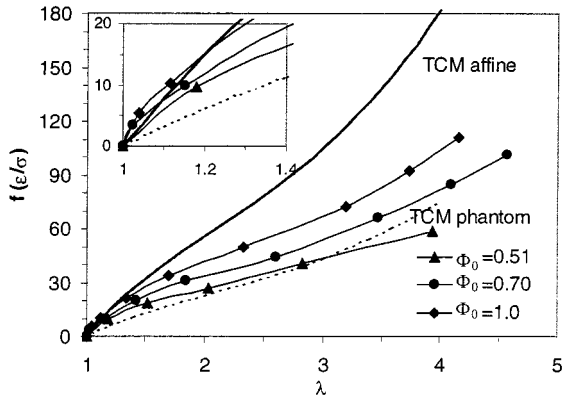

Figure 7. Force−strain relations for 50-mer networks cured at different precursor chain concentrations. Theoretical predictions based on the three-chain model and phantom-network models are also shown for comparison.

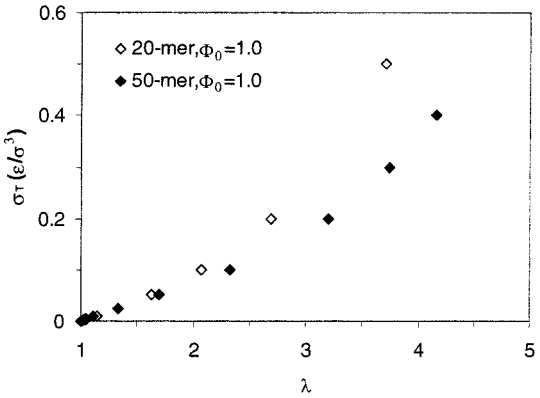

Figure 8. Stress−strain relations for 20-mer and 50-mer networks cured at $\Phi_0 = 1.0$.

concentration Φ_0 ($>c^*$). The best fit to the data yields scaling relations of the form $\Phi_{eq} \sim \Phi_0^{\zeta}$:

$$\Phi_{eq} \sim \Phi_0^{0.25} \quad \text{for 20-mer networks} \tag{10}$$

$$\Phi_{eq} \sim \Phi_0^{0.55} \quad \text{for 50-mer networks} \tag{11}$$

Note that the scaling exponent ζ increases as the length of the precursor chains increases. For swelling in a good solvent, scaling theory for entanglement-dominated networks predicts that[36]

$$\Phi_{eq} \sim \Phi_0^{1.0} \tag{12}$$

As expected, 50-mer chains are not long enough to be in the entanglement-dominated regime. Assuming that our models can represent the behavior of PDMS systems, then one Kuhn segment is equivalent to approximately 6.1 repeat units in a PDMS chain (according to ref 37). The molecular weights of the 20-mer and 50-mer chains in our simulations are then estimated to be 9000 and 22 500, respectively. In experiments, higher ζ values were observed for PDMS networks with precursor chains of commensurate molecular weights (0.56 for $M_n = 9900$ and 0.73 for $M_n = 30\,200$, where M_n stands for number-average molecular weight). The discrepancy between simulation and experimental results may be partially due to differences in network sample preparation. In experiments, the precursor chains were cured for the same prescribed amount of time; the differences in the structural properties at different Φ_0 may not be negligible. In simulation, the run was stopped at the point where structural properties were as similar as possible; the curing times for different values of Φ_0 were usually significantly different. If simulated networks were cured for the same amount of time used for $\Phi_0 = 1.0$, networks formed at lower Φ_0 would have more defects (in the form of pendent chains and loops) and less elastic material; this would lead to more swelling (a lower Φ_{eq} than in Figure 6) and a larger apparent ζ. We then argue that the simulated exponents ζ reflect more directly the differences in degree of entanglement associated with different values of Φ_0.

3.3. Uniaxial Deformation. The simulated force vs strain curves at uniaxial extension are shown in Figure 7 for 50-mer networks prepared at different values of Φ_0. All curves are slightly convex at small strain and exhibit an upturn of the force at high strain; such features are consistent with experimentally observed force−strain relations. At the same tensile force, the network formed at higher Φ_0 has a smaller strain ratio because of a greater content of trapped entanglements. Theoretical calculations were also performed for the three-chain model (TCM); under the assumption of affine deformation, the tensile force under strain is predicted to be[5]

$$f_{TCM} = \frac{nk_BTL_{x,0}L_{y,0}}{3V}\frac{R_{e,0}}{\sigma} \times \left[\mathcal{L}^{-1}\left(\frac{R_{e,0}\lambda}{N\sigma}\right) - \lambda^{-3/2}\mathcal{L}^{-1}\left(\frac{R_{e,0}\lambda^{-1/2}}{N\sigma}\right)\right] \tag{13}$$

where T is the temperature and $\mathcal{L}^{-1}$ is the inverse Langevin function. The values of $R_{e,0}$, the average end-to-end distance of the network chains at undeformed state, are obtained from simulations. The phantom-network prediction of the TCM can be obtained simply by multiplying f_{TCM} by the cyclic rank per network chain ξ/n (estimated to be about 0.41 for the samples used in our simulations). Overall, our results are consistent with the view[9] already examined in section 3.1 that entanglements effectively reduce cross-link fluctuations; thus, as the degree of entanglements decreases (i.e., as Φ_0 decreases), a network should gradually change from having an affine-model type of behavior to having a phantom-model type of behavior (as seen in Figure 7). Indeed, at moderate strains ($1.2 < \lambda < 3.0$), the affine model overpredicts the simulated tensile forces, while the phantom network model underpredicts such values. At small strains (see Figure 7, inset), however, the affine model curve lies beneath those for networks formed at $\Phi_0 = 1.0$ and 0.70, indicating that TCM underpredicts the modulus when entanglements are significant. A more detailed discussion of the behavior of the simulation results at small deformation is given shortly. At large strain, the abrupt upward curvatures in the TCM curves originate from the finite extensibility of the network chains in affine deformation. The departures of simulation curves from TCM predictions in this region are partly due to nonaffine deformation. These results are consistent with reported simulation data[38] that showed that the TCM is only accurate for small λ where the chain-force law is linear (i.e., where chains are effectively Gaussian[5]). Similar results (not shown) were observed for the 20-mer networks.

Figure 8 shows a stress−strain plot of networks with different precursor chain length formed at $\Phi_0 = 1.0$. It

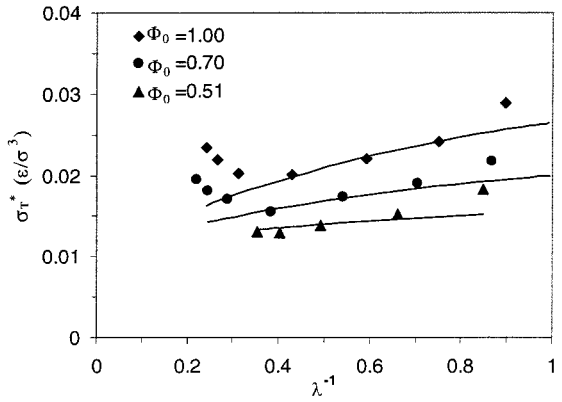

Figure 9. Mooney−Rivlin plot for the uniaxial deformation of 50-mer networks formed at different precursor chain concentrations. The solid lines are best fits to the RP model; see text for details.

can be seen that for the same stress σ_T the 20-mer network deforms less than the 50-mer network; although the 50-mer network has more trapped entanglements than the 20-mer network, the latter has a higher cross-link density than the former. The dependence of the stress−strain curves on precursor chain length and Φ_0 is consistent with the swelling behavior described before.

Figure 9 shows the simulated stress and strain data for the 50-mer networks in the familiar Mooney−Rivlin form where

$$\sigma^*_T(\lambda^{-1}) = \frac{\sigma_T}{\lambda^2 - \lambda^{-1}} \tag{14}$$

The solid lines are the best fits to Rubinstein and Panyukov's (RP) nonaffine model,[39] where the following stress−strain relation was used:

$$\sigma^*_T = G_c + \frac{G_e}{\lambda - \lambda^{1/2} + 1} \tag{15}$$

G_c is the modulus of the phantom network, which accounts for the effect of the chemical cross-links, while G_e represents the entanglement contribution to the modulus, which is essentially equal to the plateau modulus of entangled polymer solutions or high molecular weight melts. The fitting parameters found are $G_c \approx 0.0115$ (units of ϵ/σ^3), valid for all three sets of data, and $G_e \approx 0.015$ for the network formed at $\Phi_0 = 1.0$, $G_e \approx 0.0085$ for the network formed at $\Phi_0 = 0.70$, and $G_e \approx 0.004$ for the network formed at $\Phi_0 = 0.51$. The value of G_c is close to the shear modulus from the affine model:

$$G_{affine} = k_B T n w_{elast}/V \approx 0.0145 \tag{16}$$

where w_{elast} is the fraction of the elastically effective material. From simulation data, the dependence of G_e on Φ_0 can be described by the expression $G_e \sim \Phi_0^{1.96}$, which is reminiscent of that of the plateau modulus in polymer solutions,[40] i.e., $G_e \sim \Phi_0^{2.3}$. The RP model describes simulation data for uniaxial extension well, except for large λ (where the upturn in σ^*_T vs λ curve occurs) and for $\lambda \to 1$ (where data are less reliable).

The simulation data for both extension and compression simulations of 50-mer networks are presented in a Mooney−Rivlin plot in Figure 10a. The prediction of the RP model in the compression region is based on values

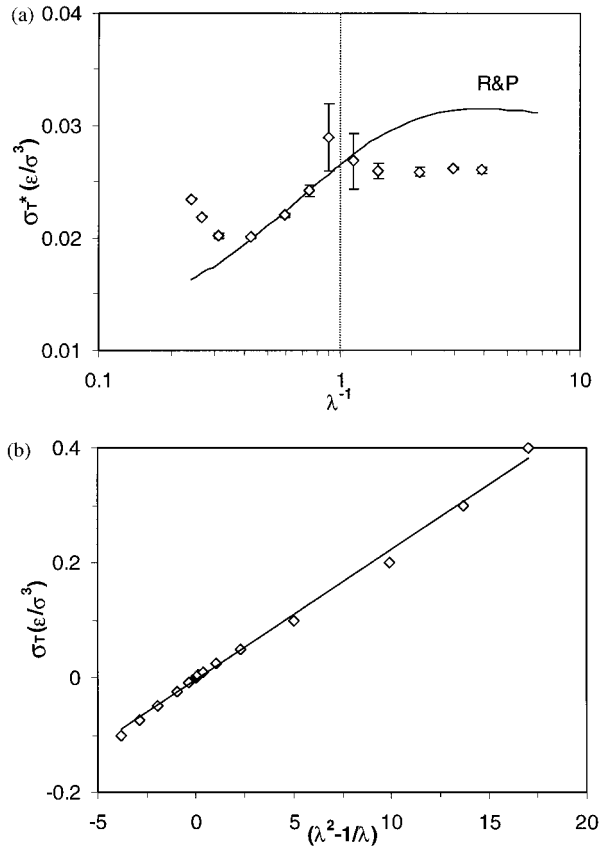

Figure 10. (a) Comparison of simulation data (diamonds) with predictions of the RP model (solid line) for the Mooney−Rivlin representation of uniaxial extension and compression for 50-mer networks formed at melt conditions. (b) Stress σ_T against $(\lambda^2 - \lambda^{-1})$ for the same set of data. The straight line is a linear fit to the data.

of G_c and G_e (see eq 15) regressed from the stretching data. Not surprisingly, the RP model overestimates the reduced stress σ^*_T in the compression region; a similar discrepancy has also been observed when experimental data were compared to predictions from this model.[41] In Figure 10b, the simulated stress−strain data are presented as σ_T vs $(\lambda^2 - \lambda^{-1})$; it can be seen that the linear relation implied by the affine and phantom models is only approximately satisfied.

The elastic modulus can be indirectly estimated from the RP model by letting $\lambda \to 1$; i.e., $G = G_c + G_e$. Note that G is just the value of σ^*_T at the intercept between the RP curve and the $\lambda^{-1} = 1$ line in Figure 9 and that a similar result would be obtained if we find the intercept between the best-fit line to the compression data and the $\lambda^{-1} = 1$ line in Figure 10a. For the 50-mer networks we obtain $G = 0.0265$, 0.0200, and 0.0155 (in units of ϵ/σ^3) for $\Phi_0 = 1.0$, 0.70, and 0.51, respectively. These values of G are larger than $G_{affine} = 0.0145$ obtained from the TCM affine model (eq 13), consistent with a comparison based on the moduli estimated from the initial slope of the force−strain curves shown in the inset of Figure 7 (albeit such slopes are not very reliable given the large uncertainty of simulated deformations at small strain). These results are also consistent with the notion that, for a network with a given number of elastic chains, the modulus of a realistic entangled network should be higher than predicted by the affine model that neglects entanglement effects. At small deformations then, entanglements make the network behave as if it has an effectively higher concentration

Table 2. Conformational Properties of Elastic Chains during Uniaxial Deformation in the *z* Direction for 50-mer Network Cured at $\Phi_0 = 1.0$[a]

	$R_{e,xy}^2$	$R_{e,z}^2$	$R_{g,xy}^2$	$R_{g,z}^2$	$R_{e,xy}^2/R_{g,xy}^2$	$R_{e,z}^2/R_{g,z}^2$	$\lambda_{z,m}$	λ
initial state, $P_z = 3.0$	30.50	29.47	4.90	4.71	6.22	6.26	1.0	1.0
$P_z = 2.99$	27.8(5)	35.0(8)	4.64(4)	5.3(1)	5.99	6.6	1.09	1.11
$P_z = 2.9$	16.27	120.7	3.23	13.42	5.04	8.99	2.02	2.33
$P_z = 2.8$	12.48	212.9	2.70	22.34	4.62	9.53	2.69	3.20
$P_z = 2.6$	9.7(1)	342(2)	2.22(2)	34.2(2)	4.37	10.0	3.41	4.16

[a] The numbers in parentheses represent the simulation uncertainties in the last digits.

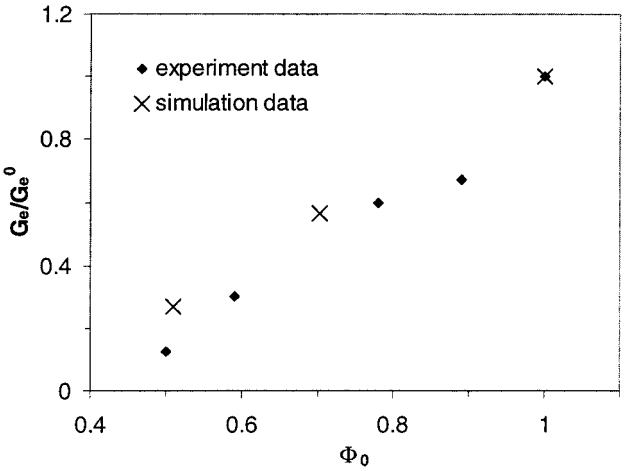

Figure 11. Variation of the entanglement contribution to the modulus, G_e, as a function of the volume fraction of precursor chain at curing (Φ_0): experimental data are for end-linked PDMS network with precursor chains of $M_n = 30\,200$ and simulation data are for our 50-mer model networks. The values of G_e are normalized by G_e^0, the value of G_e corresponding to $\Phi_0 = 1.0$.

of cross-links. The fact that this situation reverses as strain increases, i.e., the stress predicted by the affine model becomes larger than those of our simulated entangled networks for a given λ (as in Figure 7), indicates that entanglements do not act as chemical cross-links at high strain. As the network stretches, entanglement nodes may slip, and their contribution to the stress decreases. When that contribution can no longer compensate for the decrease in stress due to the fluctuations of the cross-links (accounted for in the phantom model), the stress drops below the value predicted by the affine model. Note that, in both TCM theories considered here, the elastic chains deform affinely between cross-links which are either fixed (affine model) or fluctuating (phantom model). We will show below, however, that our simulated elastic chains do not deform affinely past $\lambda = 1.1$.

Experimental force vs strain data at uniaxial extension were also examined for end-linked PDMS networks formed from precursor chains with a molar mass of 30 200 g/mol at different concentrations (see ref 30 for the details of the synthesis). G_c and G_e were obtained by fitting experimental data to eq 15; Figure 11 shows a comparison between experimental G_e vs Φ_0 curves and those from the simulation of 50-mer networks. To make this comparison, experimental and simulation values of G_e have been reduced by the corresponding value of G_e for the network prepared at melt conditions ($\Phi_0 = 1$). Experimental and simulation data sets agree relatively well and show the expected trend of G_e increasing with Φ_0. The experimental and simulation-based curves of G_c vs Φ_0, however, are dissimilar. While a unique value of G_c is consistent with simulation data (indicating identical content of elastic chains or chemical cross-links), the values of G_c from experiment appear to increase with Φ_0 (results not shown), suggesting that low-Φ_0 networks may have had less elastic material. The latter observation is consistent with an apparent exponent in $\Phi_{eq} \sim \Phi_0^{\xi}$ being larger for experiments than for simulation as alluded to earlier.

The consistency between the elastic modulus derived from uniaxial deformation simulations and equilibrium swelling behavior can be probed by using the following form of the Flory–Rehner equation:[42,43]

$$\ln(1 - \Phi_{eq}) + \Phi_{eq} + \chi\Phi_{eq}^2 = v_1 G\left[\frac{\Phi_{eq}}{2} - \Phi_{eq}^{1/3}\right] \quad (17)$$

where χ is the polymer–solvent interaction parameter (set to zero for our athermal system) and v_1 is the molar volume of solvent. Under the assumption of a monomeric explicit solvent (in line with Flory theory), v_1 in the off-lattice system is estimated to be $1/\rho_{melt}$. Using the values of G from the fits to the RP model, the predicted values of Φ_{eq} were also plotted in Figure 6 along with the simulated data. Calculated values are not in agreement with simulated data but correctly capture their trend. The theory seems to consistently overestimate Φ_{eq} (i.e., predict less swelling) relative to simulation results; aside from errors linked to the approximations invoked by the theory, such deviations are consistent with the idea that the implicit solvent employed in our simulations behaves as a better solvent than an explicit monomeric fluid at finite densities (as in Figure 3).

The conformational properties of elastic chains in the 50-mer network formed at $\Phi_0 = 1.0$ are presented in Table 2. The ratio of $\langle R_{e,z}^2\rangle/\langle R_{g,z}^2\rangle$ increases as the deformation ratio increases, suggesting that the chain ends of the elastic chains deform to a greater extent than the inner segments; this observation is consistent with the results from an on-lattice MC simulation.[27] The ratio of $\langle R_{e,xy}^2\rangle/\langle R_{g,xy}^2\rangle$ decreases as the deformation ratio increases, suggesting that the chains tend to collapse in the transverse directions *x* and *y* during the deformation. This trend is different from that found in ref 27 where that ratio remains almost constant at 6, indicating that the chains are behaving in a Gaussian-like manner in the *x* and *y* directions; such a Gaussian-like behavior is likely to be due to the fact that the network in ref 27 actually swelled upon stretching (to keep the cross section area constant). At small strain (e.g., for $P_z = 2.99$), the microscopic deformation ratio $\lambda_{z,m}$ is close to the macroscopic ratio λ. At larger strains, however, these two ratios are quite different, and the values of λ are always greater than those of $\lambda_{z,m}$, indicating that the deformation is nonaffine and implying a scenario of unfolding substructures.[23,44] Similar results were obtained for 50-mer networks formed at other initial concentrations and for 20-mer networks (results not shown). Figure 12 shows a series of "snapshots" of a 50-mer network at different degrees of deformation: $\lambda = 1$

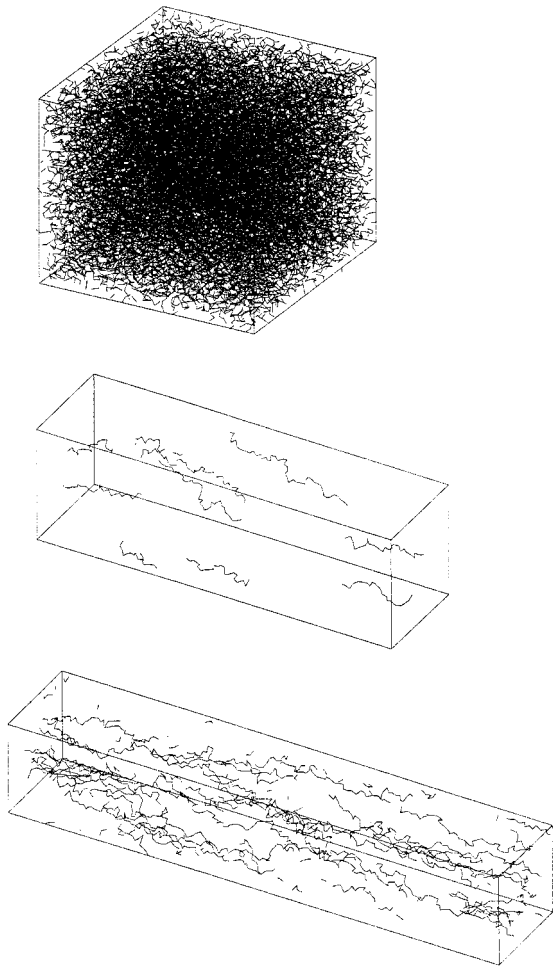

Figure 12. Selected snapshots of a 50-mer network undergoing uniaxial extension. For clarity, only chain backbones are displayed. The upper image corresponds to the initial undeformed state ($\lambda = 1$) and shows all the network chains. The two lower images show systems with $\lambda = 2.3$ and 3.2, respectively, where only those chains whose end-to-end distance is at least 45% of the maximum contour length are shown. The apparent interruption in the chain conformations is due to the periodic boundary condition.

(undeformed state), $\lambda = 2.3$, and $\lambda = 3.2$. While all the network chains are shown in the undeformed state, only those with an end-to-end distance greater than 45% of the maximum contour length are shown in the deformed states. It is seen that as λ increases, more chains are severely distorted (more extended) and tend to align with the strain direction; a more quantitative analysis of this phenomenon is elucidated in the following discussion of segment order parameter.

In Figure 13, the segment order parameter S is plotted as a function of $(\lambda^2 - \lambda^{-1})$ for the 50-mer networks. Interestingly, simulation data agree well with the phantom model prediction $S \propto (\lambda^2 - \lambda^{-1})$ in the range of λ studied (from 1.0 to 4.5), even though deviations were observed in the analysis of deformation ratios and stress−strain relations (see Figure 10b). The difference in the slopes of the linear fits reflects the difference in the extent of entanglement: a network formed at higher Φ_0 has more entanglements, which translates into a steeper slope. In recent simulations studies on the stress relaxation in polymer melts[45] and elastomeric networks,[46] it was found that stress is proportional to S, i.e., $\sigma_T = CS$, where C is a constant. The validity of such a relation has been explained by

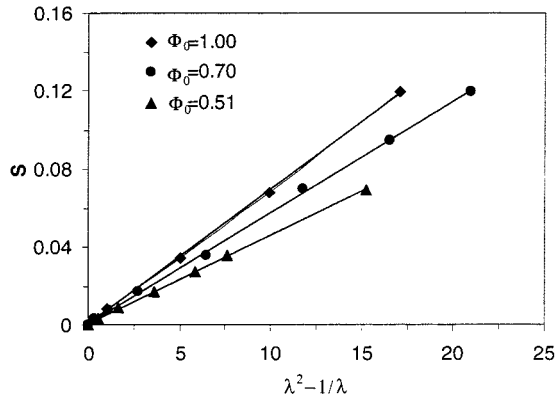

Figure 13. Segment order parameter S as a function of $(\lambda^2 - \lambda^{-1})$ for 50-mer networks.

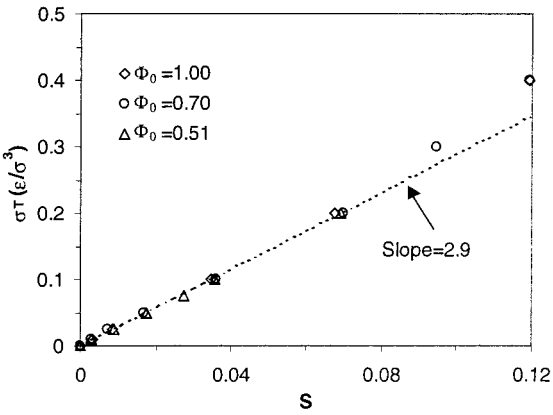

Figure 14. Stress σ_T as a function of segment order parameter S. The straight line is a linear fit to the data for $\sigma_T \leq 0.2$.

an "atomic-level" physical picture of stress production,[45] wherein nonbonded repulsive interactions have a dominant contribution to σ_T while bonded interactions have a smaller (and negative) contribution to it. While those studies focused on the dynamics of stress relaxation, the same mechanisms for stress production must operate in the "equilibrium" state of strained polymer networks and thus lead to $\sigma_T = CS$.[45] As shown in Figure 14, the linear correlation between stress and the segment order parameter does hold for our systems for small stresses (for $\sigma_T < 0.2$); however, some deviations are observed at high stresses. The value of the stress-bond orientation coefficient $C = 2.9\epsilon\sigma^{-3}$ found here is surprisingly similar to the value found in ref 45 ($C = 3.5$) despite the differences in the molecular models used in the two studies. The fact that σ_T vs S data for our 50-mer networks essentially collapse into a master curve over the entire range of conditions examined and regardless of strain and degree of entanglement supports the view that the stress σ_T originates primarily from the (entropic) excluded-volume interactions registered on an atomic or a bead basis (the degree of model coarse graining being unimportant). Configurational entropy effects contributing (to varying degrees) to σ_T can then be fully accounted for through their impact on bond orientation.

4. Conclusions

Through the combination of on-lattice simulations for network preparation and off-lattice simulations for network deformation, the effect of entanglements on network elastic behavior has been examined. The networks were prepared by end-linking a preequilibrated

system of monodisperse precursor chains (20-mers or 50-mers) at three different volume fractions, $\Phi_0 = 1.0$, 0.70, and 0.51. To isolate entanglement effects, the reaction time is controlled in such a way that the differences in network structural properties (chemical topology) are minimized among samples formed at different Φ_0. The resulting networks, having different degree of entanglements, were then subjected to deformations using off-lattice isobaric and isostress ensemble simulations; highly efficient cluster volume moves were used to change the dimensions of the system.

Simulated swelling data clearly reflect the effect of entanglements: networks formed at higher Φ_0 swell less than those formed at lower Φ_0. It was found that exponent ζ in $\Phi_{eq} \sim \Phi_0^{\zeta}$, describing the Φ_0 dependence of the equilibrium swelling (Φ_{eq}), increases with precursor chain length; this indicates that the effect of entanglements becomes more significant as network chains becomes longer. As expected, however, the value of ζ for 50-mer networks is smaller than that for entanglement-dominated systems ($\zeta = 1.0$) since 50-mer chains are only slightly larger than the chain entanglement size of 38-mer.

The simulated force−strain curves show that a network formed at a higher Φ_0, i.e., a more entangled network, requires a higher tensile force to attain a given deformation ratio λ. The conformational properties of elastic chains reveal a nonaffine behavior at large strains. It was also found that the order parameter S of the deformed networks depends linearly on $(\lambda^2 - \lambda^{-1})$, and the slope can be directly related to the degree of entanglement. Furthermore, a unique quasi-linear relation was found between S and the deformation stress, regardless of degree of entanglement. Such a relation supports the view of an atomic-level mechanism of stress production. By fitting simulated stress−strain data to the RP nonaffine model, it was found that with the same chemical modulus (G_c) the model fits extension simulation data well and gives values of the entanglement contribution to the modulus (G_e) that increase with Φ_0. The dependence of G_e on Φ_0 obtained from simulation data was found to be consistent with that obtained from experimental data for PDMS networks of commensurate molecular weight. For networks with identical number of elastic chains, our analysis shows that the stress at small strains (i.e., elastic modulus) for our simulated entangled networks is greater than that predicted by the affine model which does not account for entanglement effects. Such a trend is reversed, however, as strain increases and slippage ensues; i.e., unlike the elastic effect associated with chemical cross-links, the effect of entanglements is found to depend strongly on strain.

Altogether, our simulation data show a consistent and significant effect of entanglements on both swelling and uniaxial deformation behavior of networks. The simulation methods and analysis presented here have been shown to provide a powerful means to quantify the effect of entanglements in model elastomers; such tools can be easily adapted to examine more complex systems. This work thus provides a starting point to the systematic study of the effect of topologic and chemical complexity on the elastic properties of elastomers. Some of our ongoing efforts are aimed at locating and monitoring the evolution upon deformation of low-mobility regions in the network[47] (which can be associated with entanglements). In addition, simulations of networks made up of semiflexible chains are under way since these could provide new insights into the onset of strain-induced order−disorder transitions in elastomers.

Acknowledgment. This work was supported by the Polymers Program of the National Science Foundation, Grant DMR-0078863. The authors are grateful to N. Gilra and Prof. A. Z. Panagiotopoulos for the codes for the BFM, to Prof. M. Duncan for valuable comments, and to C. Wong for the experimental data presented in Figure 11.

References and Notes

(1) Flory, P. J.; Rehner, J. *J. Chem. Phys.* **1943**, *11*, 512.
(2) Wall, F. T. *J. Chem. Phys.* **1943**, *11*, 527.
(3) James, H. M.; Guth, E. *J. Chem. Phys.* **1943**, *11*, 455.
(4) James, H. M.; Guth, E. *J. Chem. Phys.* **1947**, *15*, 669.
(5) Treloar, L. R. G. *The Physics of Rubber Elasticity*; Clarendon Press: Oxford, England, 1958.
(6) Ronca, G.; Allegra, G. *J. Chem. Phys.* **1975**, *63*, 4990.
(7) Flory, P. J. *J. Chem. Phys.* **1977**, *66*, 5720.
(8) Erman, B.; Flory, P. J. *J. Chem. Phys.* **1978**, *68*, 5363.
(9) Flory, P. J.; Erman, B. *Macromolecules* **1982**, *15*, 800.
(10) Edwards, S. F. *Proc. Phys. Soc.* **1967**, *92*, 9.
(11) Edwards, S. F. *Br. Polym. J.* **1977**, *9*, 140.
(12) Eichinger, B. E. *Annu. Rev. Phys. Chem.* **1983**, *34*, 359.
(13) Heinrich, G. *Adv. Polym. Sci.* **1988**, *85*, 33.
(14) Edwards, S. F.; Vilgis, T. A. *Rep. Prog. Phys.* **1988**, *51*, 243.
(15) Termonia, Y. *Macromolecules* **1989**, *22*, 3633.
(16) Duering, E. R.; Kremer, K.; Grest, G. S. *Phys. Rev. Lett.* **1991**, *67*, 3531.
(17) Duering, E. R.; Kremer, K.; Grest, G. S. *J. Chem. Phys.* **1994**, *101*, 8169.
(18) Everaers, R.; Kremer, K. *Macromolecules* **1995**, *28*, 7291.
(19) Everaers, R.; Kremer, K. *Phys. Rev. E* **1996**, *53*, R37.
(20) Hölzl, T.; Trautenberg, H. L.; Göritz, D. *Phys. Rev. Lett.* **1997**, *79*, 2293.
(21) Everaers, R. *New J. Phys.* **1999**, *1*, 12.1−12.54.
(22) Sommer, J.-U. *Macromol. Symp.* **1994**, *81*, 139.
(23) Trautenberg, H.; Sommer, J.-U.; Göritz, D. *J. Chem. Soc., Faraday Trans.* **1995**, *91*, 2649.
(24) Escobedo, F. A.; de Pablo, J. J. *J. Chem. Phys.* **1996**, *104*, 4788.
(25) Escobedo, F. A.; de Pablo, J. J. *J. Chem. Phys.* **1997**, *106*, 793.
(26) Kenkare, R.; Hall, C. K.; Khan, S. A. *J. Chem. Phys.* **2000**, *113*, 404.
(27) Gilra, N.; Panagiotopoulos, A. Z.; Cohen, C. *Macromolecules* **2001**, *34*, 6090.
(28) Deutsch, H.-P.; Binder, K. *J. Chem. Phys.* **1991**, *94*, 2294.
(29) Paul, W.; Binder, K.; Heermann, D.; Kremer, K. *J. Phys. II* **1991**, *1*, 37.
(30) Sivasailam, K.; Cohen, C. *J. Rheol.* **2000**, *44*, 897.
(31) Kenkare, N. R.; Smith, S. W.; Hall, C. K.; Khan, S. A. *Macromolecules* **1998**, *31*, 5861.
(32) Gilra, N.; Cohen, C.; Panagiotopoulos, A. Z. *J. Chem. Phys.* **2000**, *112*, 6910.
(33) Allen, M. P.; Tildesley, D. J. *Computer Simulation of Liquids*; Clarendon: Oxford, 1987.
(34) Kuhn, W.; Grün, F. *Kolloid Z.* **1942**, *101*, 248.
(35) Flory, P. J. *Principles of Polymer Chemistry*; Cornell University: Ithaca, NY, 1953.
(36) Obukhov, S. P.; Rubinstein, M.; Colby, R. H. *Macromolecules* **1994**, *27*, 3191.
(37) Shibanov, Y. D. *Polym. Sci. U.S.S.R.* **1989**, *31*, 2653.
(38) Gao, J.; Weiner, J. H. *Macromolecules* **1991**, *24*, 1519.
(39) Rubinstein, M.; Panyukov, S. *Macromolecules* **1997**, *30*, 8036.
(40) Colby, R. H.; Rubinstein, M. *Macromolecules* **1990**, *23*, 2753.
(41) Roland, C. M.; Mott, P. H. *Macromolecules* **1998**, *31*, 4033.
(42) Flory, P. J.; Rehner, J. *J. Chem. Phys.* **1943**, *11*, 521.
(43) Patel, S. K.; Malone, S.; Cohen, C.; Gillmor, J. R.; Colby, R. H. *Macromolecules* **1992**, *25*, 5241.
(44) Candau, S.; Bastide, J.; Delsanti, M. *Adv. Polym. Sci.* **1982**, *44*, 28.
(45) Picu, R. C.; Loriot, G.; Weiner, J. H. *J. Chem. Phys.* **1999**, *110*, 4678.
(46) Bergström, J. S.; Boyce, M. C. *Macromolecules* **2001**, *34*, 614.
(47) Gao, J.; Weiner, J. H. *J. Chem. Phys.* **1995**, *103*, 1621.

MA012048I